# Chapter 6

## Structural, optical and electrical studies of Ag-ZnO nanocomposites

*In this chapter, we report the synthesis of pure ZnO and plasmonic Ag-ZnO nanocomposites by a facile precipitation method. X-ray diffraction analysis is done for the investigation of phase purity of the synthesized samples. The crystallite size and lattice strain of the samples are obtained by Debye-Scherrer and Williamson–Hall analysis. The UV-Vis absorption spectra of the Ag-ZnO nanocomposites reveal an increased optical absorption in the UV region, which suggests that Ag-ZnO nanocomposite can be used as a UV detector. Furthermore, I-V characteristics of the samples have been measured in an applied bias range of -2V to 2V under dark and UV illumination (λ=365 nm). A significant increase in the photocurrent and a three-fold enhancement in the responsivity values in 13.7 wt. % Ag-ZnO nanocomposite as compared to the bare ZnO are attributed to the localized surface plasmon resonance phenomena and strain reduction.*

## 6.1 Introduction

Over the past few decades, nano-sized metal-oxide semiconductors have gained much attention from the research fraternity due to their versatile manifold properties like ferroelectric, magnetic, dielectric, spectroscopic, luminescence, and varying conductivity. Extensive research has been done to investigate and explore these properties for a plethora of applications such as anti-pollutant, toxic gas detectors [176,177], photovoltaic devices, fuel cells, electrodes [178], display devices [179] etc.

Among several metal oxides such as $SnO_2$, $In_2O_3$, $TiO_2$, ZnO, NiO, etc., zinc oxide (ZnO), an II-VI compound semiconductor, is very attractive owing to its direct wide bandgap (3.3 eV), large exciton binding energy (60 meV), high thermal, mechanical and chemical stability and exhibits unique structural, optical and electrical properties [180,181]. It is considered as a natural n-type semiconductor having wurtzite hexagonal structure with space group $P6_3mc$. ZnO is a very encouraging candidate for applications in diverse fields such as photonics [182], gas sensors [183,184], biomedical applications [185], photocatalytic activity [186], etc.

Metallic nanostructures having sub-wavelength dimensions exhibit localized surface plasmon resonance (LSPR), increasing the optical absorption and near-field enhancement in the neighbourhood of the nanoparticles. The absorption can be increased in two ways- (a) by the coupling of incident electromagnetic radiation with the localized surface plasmons of the metallic nanoparticles, which increases the scattering cross-section of the metallic nanoparticles as well as the optical path length of the incident light and (b) by the near field enhancement arising due to the trapping of light by surface plasmon excitation in the metallic nanoparticles [187,188].

Among several noble metal (Ag, Au, Pt, Cu etc.) nanoparticles, Ag nanoparticle is predominantly chosen as a plasmonic material owing to its lower interband losses at optical frequencies and ubiquitous optical, electrical and chemical properties [189]. Moreover, it's low cost, shape, and size-controlled synthesis methods open up new possibilities and make it a better candidate for its incorporation in the diverse arena like Surface-Enhanced Raman Spectroscopy (SERS), high catalytic material, antibacterial and biosensor material, cosmetics and electronic components [190,191].

Metal nanostructures along with metal-oxide semiconductors i.e. metal-semiconductor nano-heterostructures are the most intriguing nanostructures because they exhibit unique physical and chemical properties and potential applications in developing various nano-optoelectronic devices, ascribed to localized surface plasmon resonance of metallic nanoparticles arising due to the adsorption of metal nanoparticles on the semiconducting active material [176,192]. These heterostructures exhibit unprecedented properties and multiple functionalities, which are unachievable by metal nanoparticles or oxide materials alone [192]. The Ag–ZnO nanocomposite is an exquisite metal-semiconductor nano- heterostructured material and finds application in various fields such as- optoelectronic devices [193], luminescent material [194], antibacterial application [195], plasmonic application [196], sensor selectivity [197], spintronics [198] and UV photodetection [199], etc.

Extensive efforts have been made to synthesize various compositions of Ag-ZnO nanocomposites. Tarek et.al have synthesized Ag-ZnO nanocomposite containing 50 wt.% Ag with respect to ZnO via photoreduction method and studied its structural and emission properties [200]. Zheng et.al have reported Ag/ZnO nanocomposite, in which Ag content was up to 20 mol% of ZnO and explained its photocatalytic properties [201].

Further, Yang et.al have also synthesized Ag-ZnO heterostructures with Ag up to 15 mol% of ZnO, assisted by UV irradiation, to explain its photocatalytic activity [202].

In recent years, UV detection has become a matter of great importance not only for several commercial, military, and scientific domains but also for human health, as it causes several skin and eye-related issues such as- skin cancer, cataracts [203], etc.

In this chapter, we have synthesized Pure ZnO and compositions of Ag-ZnO nanocomposite material by a facile sol-gel chemical process and studied their structural, optical, and electrical properties for application in UV photodetection. To date, various methods have been availed to synthesize Ag-ZnO nanocomposites such as- solvothermal, hydrothermal [201,204], gel-combustion route [205], mechanochemical combustion technique [206], sol-gel method [207], etc. However, most of these methods are either less efficient or they require expensive experimental setup. Therefore, in this work, we have opted for a facile modified sol-gel chemical process, which is a simple, viable, and low-cost synthesis technique. Moreover, it can be performed at room temperature and is solution-processed. It has also obtained a clear enhancement in the photocurrent upon UV illumination is ascribed to the LSPR phenomena. Our study corroborates that the Plasmonic Ag-ZnO nanocomposite material in proper composition is a suitable candidate for UV- photodetectors.

## 6.2 Experimental Details

### 6.2.1 Materials

Zinc nitrate hexahydrate ($Zn(NO_3)_2.6H_2O$, 99%, SRL chemicals), silver nitrate ($AgNO_3$, 99.9%, SRL chemicals), sodium hydroxide (NaOH, 98%, Sigma-Aldrich), ethylene glycol($(CH_2OH)_2$) and double distilled water have been used as materials for synthesis, without any further purification.

### 6.2.2 Synthesis of ZnO nanoparticles

The stoichiometric amount of $Zn(NO_3)_2.6H_2O$ was dissolved in 200 ml of double-distilled water under constant stirring for 1hour at room temperature. NaOH solution was added drop wise with constant stirring to reach a pH value of ~8. After continuing stirring for another 30 minutes, the solution was left for sedimentation overnight. The obtained supernatant was decanted and the residue was centrifuged and washed 3-4 times with double distilled water and ethanol followed by drying in an air oven at 90$^{o}$C for 12hrs. The obtained sample was annealed in air at 550$^{o}$C for 2 hrs. The flow chart for synthesis of ZnO nanoparticles is depicted in Fig. 6.1 (a).

### 6.2.3 Synthesis of Ag-ZnO nanocomposites

The Ag-ZnO nanocomposites were synthesized by a facile solution-processed process. 800 mg of previously prepared ZnO nanoparticles have been taken and then 120 mg and 200 mg of $AgNO_3$ powder were added separately to 20 ml of ethylene glycol. The reaction mixture was vigorously stirred at room temperature for 1 hr to get a homogeneous solution. The obtained black/brown precipitates were filtered and washed to remove any contaminant followed by drying and annealing in air at 90$^{o}$C for 12 hrs and 550$^{o}$C for 2 hrs, respectively. For I-V curve measurements the samples were pressed into discs using a pelletizer and then electroded with silver paste. Corresponding to the Ag content w.r.t. Ag-ZnO nanocomposite, the samples have been labeled as A15 for 8.7 wt.% Ag and A25 for 13.7 wt.% Ag throughout the chapter. The flow chart for synthesis of nanocomposites is depicted in Fig. 6.1 (b).

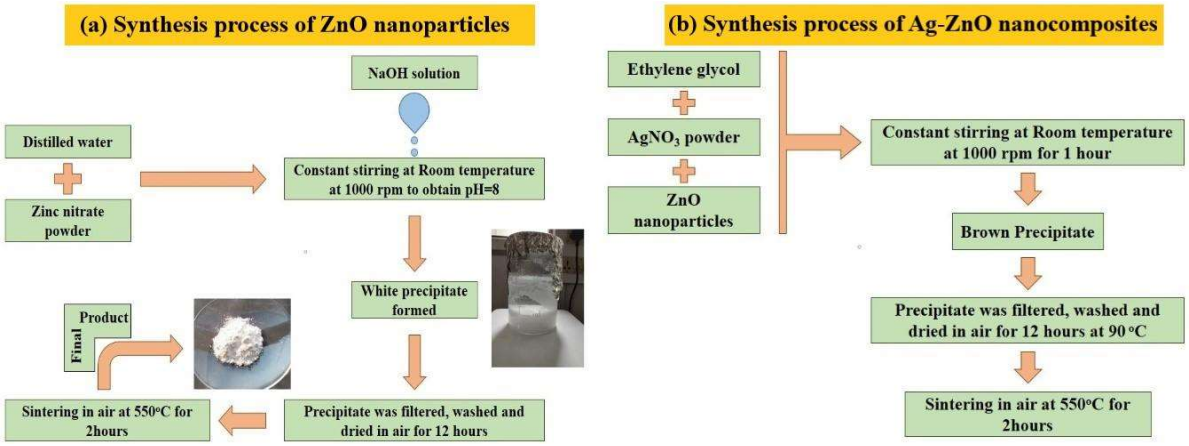


**Fig. 6. 1 (a)** Flow chart for the synthesis of ZnO nanoparticles. **(b)** Flow chart for the synthesis of Ag-ZnO nanocomposites.

### 6.3 Characterizations

The crystal structure and phase of the synthesized samples have been examined by Rigaku-MiniFlex-II DESKTOP X-ray diffractometer furnished with monochromatic Cu-$K_\alpha$ radiation ($\lambda$=0.154 nm) operating at 30 kV and 15 mA. Diffraction patterns have been recorded in the continuous scan mode in the range $2\theta = 20^o – 80^o$ at the steps of $0.02^o$. The functional group analysis was carried out by recording the FTIR spectra using JASCO FT/IR 4600 spectrophotometer in the wavenumber range 400 $cm^{-1}$ - 4000 $cm^{-1}$. The field emission scanning electron microscopy (FE-SEM) (model Nova Nano SEM 450, USA) has been performed for the grain size analysis as well as morphological study of the samples and presence of all the elements and their real contents in the samples has been confirmed by energy-dispersive X-ray (EDX) spectroscopy. Optical absorption spectroscopy of the samples ranging from 200 nm - 1000 nm was done by using JASCO V770 UV-Vis-NIR spectrophotometer. The current-voltage (I-V) characteristics of the samples have been obtained using a source meter (model B1500A from Keysight, USA) and UV lamp ($\lambda$=365 nm) in the range -2 V to 2 V at room temperature under ambient air environment.

## 6.4 Results and Discussions

### 6.4.1 X-Ray diffraction study

The Rietveld refined XRD graphs of ZnO, A15, and A25 calcined at $550^0$C in air over the range $20^o \leq 2\theta \leq 80^o$are depicted in Fig. 6.2. The XRD pattern of ZnO ascertains the hexagonal phase of the synthesized nanoparticles. The prominent diffraction reflections for ZnO are indexed as (100), (002), (101), (102), (110), (103) and (112) which matches well with the wurtzite hexagonal crystal structure of ZnO (JCPDS file no. 79-2205 (*a =3.250 Å, c =5.207 Å*)). The refinement patterns for Ag-ZnO nanocomposites, show some additional peaks indexed as (111), (200), and (220) which are marked with [#] and correspond to Ag nanoparticles (JCPDS file no. 04-0783). The three distinct peaks of Ag reveal the formation of the nanocomposite. The intensity of the peaks corresponding to Ag is found to increase with the Ag concentration. Any peak other than that of ZnO and Ag is not observed in the XRD pattern. The lattice parameters and unit cell volume of ZnO, A15, and A25 are obtained using FULLPROF software and are summarized in Table 6.1. Any remarkable variation in the lattice parameters is not observed for nanocomposites, which infer that no $Zn_{(1-x)}Ag_xO$ (solid solution) is formed. The *c/a* ratio indicates the distortion from the ideal crystal structure and for ideal HCP structure it is 1.633, however, the obtained *c/a* ratio for all samples is 1.602 and it remains the same for nanocomposites, which suggest that the tetragonality remains the same. A slight decrease in Zn-O bond length is also observed for the nanocomposites.

**Table 6.1** Rietveld refined parameters for all samples.

| **Parameters** | **ZnO** | **A15** | **A25** |
|---|---|---|---|
| *Atomic positions* | | | |
| Zn (x,y,z) | (1/3,2/3,0) | (1/3,2/3,0) | (1/3,2/3,0) |
| O (x,y,z) | (1/3,2/3,0.3724) | (1/3,2/3,0.3809) | (1/3,2/3,0.3817) |
| Angles (α, β, γ) (in degree) | (90, 90, 120) | (90, 90, 120) | (90, 90, 120) |
| *Lattice parameters for ZnO (Å)* | | | |
| a | 3.254 | 3.250 | 3.250 |
| c | 5.215 | 5.206 | 5.206 |
| *Unit cell volume ($Å^3$)* | 47.83 | 47.64 | 47.63 |
| *c/a ratio* | 1.602 | 1.602 | 1.602 |
| *Atomic Packing Fraction* | 0.754 | 0.754 | 0.754 |
| *Bond lengths (Å)* | | | |
| O-Zn | 1.993 | 1.984 | 1.987 |
| Zn-O | 1.942 | 1.976 | 1.974 |
| $R_{Factors}$ | | | |
| $R_p$ | 11.6 | 7.69 | 4.24 |
| $R_{wp}$ | 13.6 | 11.0 | 5.03 |
| $R_{exp}$ | 5.25 | 8.76 | 2.35 |
| $\chi^2$ | 6.71 | 1.59 | 4.59 |

The texture coefficient of the samples was estimated according to Harris's method [208] by applying the formula,

$$TC_{(hkl)} = \frac{I_{(hkl)}/I_{0(hkl)}}{\frac{1}{N}\sum_N I_{(hkl)}/I_{0(hkl)}} \quad (6.1)$$

Where, the measured intensity of each plane is denoted by $I_{(hkl)}$, the standard relative intensity of the corresponding plane provided by JCPDS file is denoted by $I_{0(hkl)}$ and the number of considered reflection planes is denoted by *N*. The obtained values are summarized in Table 6.2. The calculated texture coefficients ascertain that the samples are crystalline and highly textured with a preferred orientation along the (002) peak (i.e. c-axis).

**Table 6.2** Calculated Texture Coefficients of ZnO and Ag-ZnO nanocomposites for major peaks

| **Sample** | **Diffraction peaks** | | | | | | | | | |
|---|---|---|---|---|---|---|---|---|---|---|
| | **(100)** | **(002)** | **(101)** | **(111)** | **(200)** | **(102)** | **(110)** | **(103)** | **(112)** | **(201)** |
| **ZnO** | 1.26 | 1.46 | 1.09 | -- | -- | 0.81 | 0.98 | 0.76 | 0.82 | 0.82 |
| **A15** | 1.60 | 1.67 | 1.41 | 0.02 | 0.02 | 1.19 | 1.18 | 0.99 | 0.97 | 0.95 |
| **A25** | 1.60 | 1.68 | 1.39 | 0.04 | 0.03 | 1.22 | 1.17 | 0.95 | 0.96 | 0.96 |

The approximated average crystallite size (*D*) can be obtained by the Debye-Scherrer's relation where the contribution of the strain is ignored. The following relation is the well-known Scherrer's relation [209],

$$D = \frac{\lambda \times K}{\beta \times cos\theta} \quad (6.2)$$

Where the wavelength of the X-ray used is denoted by $\lambda$, K is the constant shape factor (0.9), $\theta$ is the Bragg's angle, and $\beta$ represents the full width at half maximum (FWHM) of the diffraction peaks. The evaluated *D* for ZnO, A15, and A25 are 32.38 nm, 35.77 nm, and 35.67 nm, respectively. Thus, the average crystallite size increases for nanocomposites.

The dislocation density ($\delta$), represents the amount of dislocations (defects) present in the sample and is specified as the length of dislocation lines per unit volume of the crystal, is inversely proportional to the square of crystallite size (*D*) and given by the relation,

$$\delta = \frac{1}{D^2} \tag{6.3}$$

It is inferred that the dislocation density of ZnO, A15 and A25 is 9.54 x $10^{-4}$, 7.82 x $10^{-4}$ and 7.86 x $10^{-4}$ $(nm)^{-2}$, respectively. The decrease in $\delta$ for nanocomposite ascertains the improvement in local crystal structure with Ag.

The XRD pattern can be used to approximate the lattice parameters '*a*' and '*c*' using Bragg's law,

$$2dSin\theta = n\lambda \tag{6.4}$$

Here the X-ray wavelength is denoted by $\lambda$, order of diffraction by *n*, and d represents inter planar spacing corresponding to the given Miller indices (*hkl)*.

The relation relating the Miller indices *h*, *k, l* and lattice parameters *a, c* and the inter planar spacing *d* for a hexagonal crystal structure is given by the following equation,

$$\frac{1}{d^2_{(hkl)}} = \frac{4}{3}\left(\frac{h^2 + k^2 + hk}{a^2}\right) + \left(\frac{l}{c}\right)^2 \tag{6.5}$$

Using *d* (from Eq. 6.5) in Bragg's law (Eq. 6.4) and for n=1 we get,

$$Sin^2\theta = \frac{\lambda^2}{4a^2}\left(\frac{4}{3}(h^2 + k^2 + hk) + \left(\frac{a}{c}\right)^2 l^2\right) \tag{6.6}$$

Therefore, for the (002) plane, the value of *c* can be calculated as,

$$c = \frac{\lambda}{Sin\theta} \tag{6.7}$$

Similarly, for (100) plane, the lattice constant *a* is evaluated by,

$$a = \frac{\lambda}{\sqrt{3}Sin\theta} \tag{6.8}$$

The obtained values of the lattice constants and *c/a* ratio are listed in Table 6.3.

We can calculate Zn—O bond length using the lattice parameters and positional parameter *u* for wurtzite structure by using the following equation,

$$L = \sqrt{\left(\frac{a^2}{3} + \left(\frac{1}{2} - u\right)^2 c^2\right)} \tag{6.9}$$

The positional parameter u indicates the displacement of each atom with respect to the adjacent atom along the c-axis in wurtzite structure. The following relation is used for calculating the positional parameter,

$$u = \frac{1}{3}\left(\frac{a}{c}\right)^2 + 0.25 \tag{6.10}$$

The positional parameter *u* decreases with the increase in *c/a* ratio. The calculated Zn—O bond lengths for ZnO, A15 and A25 are listed in Table 6.3.

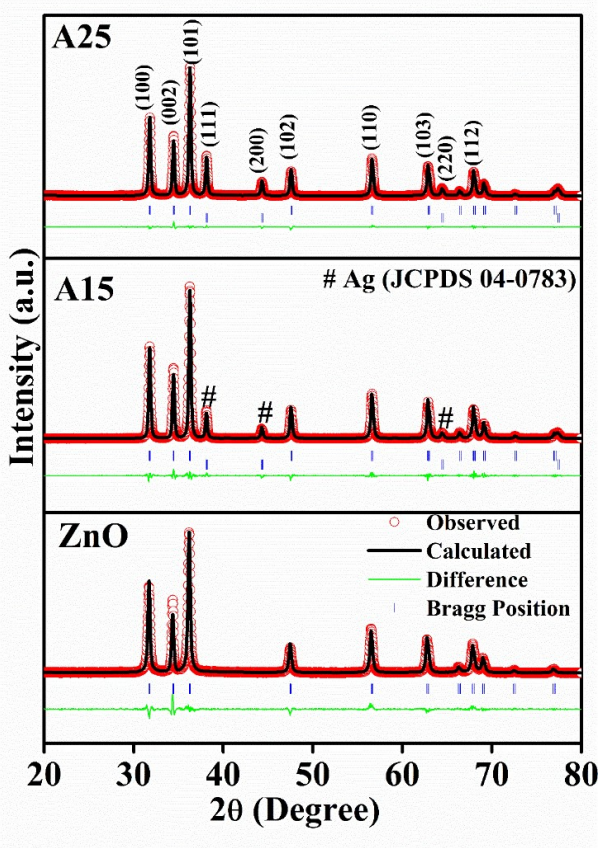


**Fig. 6.2** Stacked Rietveld refined XRD graphs for ZnO, A15 and A25.

**Table 6.3** Lattice parameters, c/a ratio, dislocation density, positional parameter and Zn—O bond length for all samples.

| Sample | Dislocation density (δ) $(nm)^{-2}$ | Lattice parameters (Å) | c/a | Positional parameter (u) | Zn-O Bond length (Å) |
|---|---|---|---|---|---|
| ZnO | $9.54 \times 10^{-4}$ | a = 3.256<br>c = 5.215 | 1.6019 | 0.3799 | 1.9815 |
| A15 | $7.82 \times 10^{-5}$ | a = 3.234<br>c = 5.183 | 1.6026 | 0.3798 | 1.9685 |
| A25 | $7.86 \times 10^{-4}$ | a = 3.239<br>c = 5.190 | 1.6023 | 0.3798 | 1.9715 |

#### 6.4.1.1 Crystallite size and strain:

Williamson-Hall (W-H) methods have been used to estimate the lattice strain ($\epsilon$) and crystallite size ($D$). The Williamson- Hall equation, which is known as uniform deformation model (UDM), is governed by the following relation,

$$\beta_{hkl} cos\theta_{hkl} = 4\epsilon sin\theta_{hkl} + \frac{K\lambda}{D} \tag{6.11}$$

Where $\theta$ is the angle corresponding to the examined peak, $\lambda$is the wavelength ($\lambda = 0.154\ nm$) of X-ray, and the shape factor $K$ is ~ 0.9 and $\beta$ is calculated FWHM obtained by deducting instrumental broadening ($\beta_{instrumental}$) from the FWHM ($\beta_{measured}$) of XRD peak pattern,

$$\beta_{hkl} = [(\beta^2_{hkl})\text{Measured} - (\beta^2_{hkl})\text{Instrumental}]^{1/2} \tag{6.12}$$

In this model, it is assumed the crystal nature is isotropic by considering the strain to be uniform in all crystallographic directions. Therefore, in UDM it is considered that the material properties remain independent to the direction of measurement. The Eq. (6.11) is a linear equation and a plot between $\beta_{hkl}\cos\theta_{hkl}$versus $4\sin\theta_{hkl}$ for all samples is shown in Fig. 6.3 (a). The crystallite size ($D$) is deduced from the y-intercept of the plot and the lattice strain ($\varepsilon$) is evaluated from the slope of the linearly fitted line. The crystallite size and microstrain variation corresponding to each sample is presented in Fig. 6.4 and tabulated in Table 6.4. It is established that the calculated microstrain for A25 is less than that of ZnO.

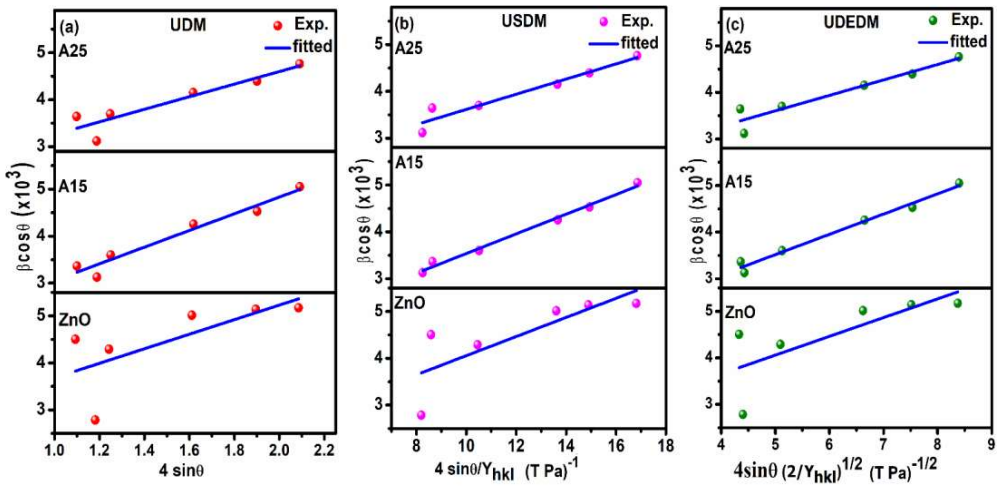


**Fig. 6.3 (a)** UDM fitting for all samples, **(b)** USDM fitting for all samples, **(c)** UDEDM fitting for all samples. The symbols show the experimental data and blue line depicts the linearly fitted line.

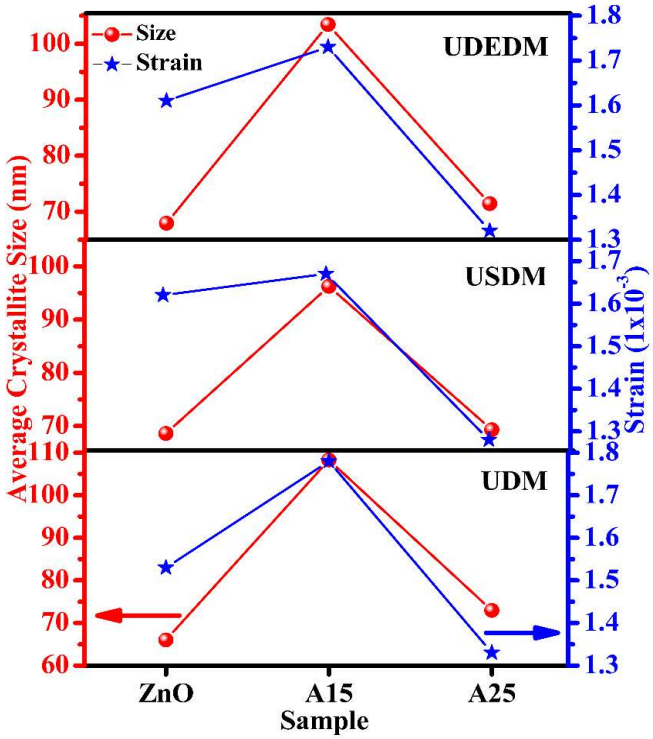


**Fig. 6.4** Comparison of average crystallite size and strain for all samples calculated by UDM, USDM and UDEDM.

**Table 6.4** Geometric parameters for ZnO and Ag-ZnO nanocomposites obtained from various models.

| Sample | Williamson-Hall method | | | | | | | | | |
|---|---|---|---|---|---|---|---|---|---|---|
| | UDM | | USDM | | | | UDEDM | | | |
| | D (nm) | Strain(ε) ($1\times10^{-3}$) | D (nm) | Young's modulus $Y_{hkl}$ (GPa) | Stress $\sigma$ (MPa) | Strain(ε) ($1\times10^{-3}$) | D (nm) | Energy density $u_{ed}$ ($KJm^{-3}$) | Strain(ε) ($1\times10^{-3}$) | Stress $\sigma$ (MPa) |
| **ZnO** | 66.0 | 1.53 | 68.61 | ~127 | 203.98 | 1.62 | 67.94 | 162.20 | 1.61 | 203.18 |
| **A15** | 108.28 | 1.78 | 96.25 | ~127 | 209.85 | 1.67 | 103.43 | 189.34 | 1.73 | 218.88 |
| **A25** | 72.95 | 1.33 | 69.30 | ~127 | 161.69 | 1.28 | 71.44 | 110.16 | 1.32 | 166.95 |

In some cases, the requirement of homogeneity and isotropic crystal nature is completely not satisfied. Therefore, equation (6.11) is further modified by incorporating anisotropic nature of strain. This model is known as uniform stress deformation model (USDM) and presumes that the lattice deformation stress is consistent in all crystallographic directions and the particles have a small microstrain in them. According to Hooke's law, the stress and strain are linearly proportional to each other and given by the relation, $\sigma = \varepsilon Y_{hkl}$, where $Y_{hkl}$ is Young's modulus or modulus of elasticity, $\sigma$ denotes the crystal stress, and $\varepsilon$ denotes anisotropic microstrain, which relies on the crystallographic directions. Substituting the value of $\varepsilon$ in Eq. (6.11),

$$\beta_{hkl}\cos\theta_{hkl} = 4\frac{\sigma sin\theta_{hkl}}{Y_{hkl}} + \frac{K\lambda}{D} \qquad (6.13)$$

The Young's modulus for a hexagonal crystal with lattice parameters *a* and *c* is obtained from the following relation,

$$Y_{hkl} = \frac{\left[h^2 + \frac{(h+2k)^2}{3} + \left(\frac{al}{c}\right)^2\right]^2}{s_{11}\left(h^2 + \frac{(h+2k)^2}{3}\right)^2 + s_{33}\left(\frac{al}{c}\right)^4 + (2s_{13} + s_{44})\left(h^2 + \frac{(h+2k)^2}{3}\right)\left(\frac{al}{c}\right)^2} \quad (6.14)$$

Where, $h$, $k$ and $l$ are the Miller indices and $s_{11}$,$s_{13}$,$s_{33}$, and $s_{44}$ represent the elastic compliances of ZnO having values 7.858 × $10^{-12}$, -2.206 × $10^{-12}$, 6.940 × $10^{-12}$ and 23.57 ×$10^{-12}$ $m^2$ $N^{-1}$, respectively.

The Eq. (6.13) is a linear equation and $\beta_{hkl}\cos\theta_{hkl}$ is plotted against $\frac{\sigma sin\theta_{hkl}}{Y_{hkl}}$ and is depicted in Fig. 6.3 (b). The intercept of Eq. (6.13) gives the crystallite size ($D$) and slope of the linearly fitted line is used to estimate uniform deformation stress $\sigma$. Table 6.4 summarizes the values of stress ($\sigma$), strain ($\varepsilon$) and crystallite size ($D$). It is found that the variation in crystallite size deduced from USDM is in good accord with UDM.

To determine the energy density $u_{ed}$ (energy per unit volume) of the nanoparticles, uniform deformation energy density model (UDEDM) is employed. In this model, as the energy density comes into play, the stress-strain relation related to proportionality constants does not remain independent. The energy density $u_{ed}$ (energy per unit volume), as per the Hooke's law, is given by $u_{ed} = (\epsilon^2 Y_{hkl})/2$. We can write W-H equation in terms of $u_{ed}$ as,

$$\beta_{hkl}\cos\theta_{hkl} = 4sin\theta_{hkl}(2u_{ed}/Y_{hkl})^{1/2} + \left(\frac{K\lambda}{D}\right) \quad (6.15)$$

The $\beta_{hkl}\cos\theta_{hkl}$ versus $4sin\theta_{hkl}(2/Y_{hkl})^{1/2}$ plot for all samples are depicted in Fig. 6.3 (c). The slope of the linearly fitted plot is used to calculate the anisotropic energy density $u_{ed}$ and from y-intercept of the plot, crystallite size (D) is determined. The lattice strain and stress can be determined by knowing the value of $u_{ed}$. The calculated crystallite size, energy density, strain, and stress are tabulated in Table 6.4. The study

from all the three models for Williamson-Hall method ascertains that the strain and stress for A25 are less than bare ZnO nanoparticles.

### 6.4.2 FT-IR study

The chemical bonding information, as well as the information of the functional groups in all the samples, is investigated by Fourier transform infrared (FT-IR) spectroscopy. Fig. 6.5 depicts the FT-IR spectra of ZnO, A15 and A25 analyzed in the range 400$cm^{-1}$-4000 $cm^{-1}$. The peaks around 450 $cm^{-1}$and 670 $cm^{-1}$ correspond to the characteristic Zn-O stretching mode while the peaks around1460 $cm^{-1}$ and 2360 $cm^{-1}$ are ascribed to the symmetric stretching of C=O and stretching vibration of $CO_2$ molecule, respectively [207,210,211]. A broad peak around 3400 $cm^{-1}$ is specified as the O-H stretching vibration of adsorbed $H_2O$ on the ZnO surface[207]. Thus, the FT-IR spectra corroborate the ZnO wurtzite structure formation in all the samples.

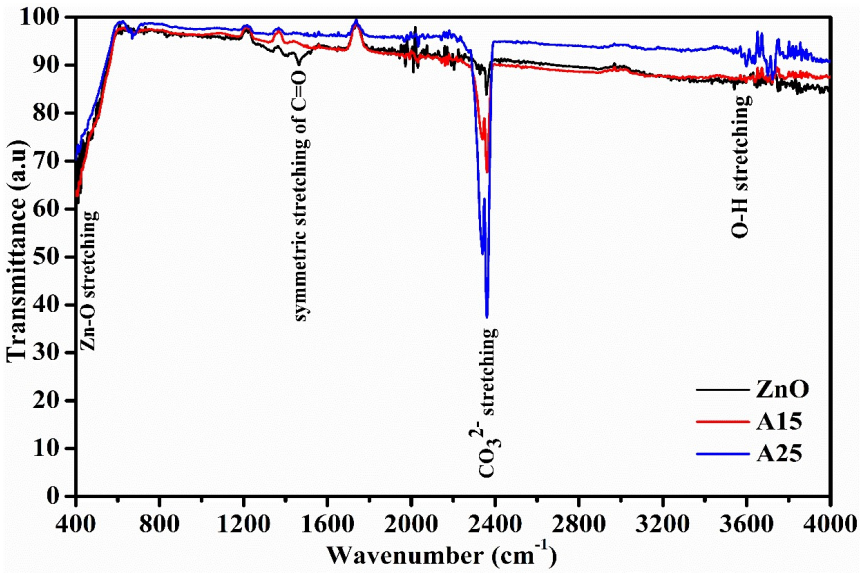


**Fig. 6.5** FT-IR spectra for all samples in the wavenumber range 400-4000 $cm^{-1}$.

### 6.4.3 Morphological and elemental study

Fig. 6.6 represents the FE-SEM micrograph of the samples. The energy-dispersive X-ray spectroscopy (EDX) has been used to confirm the presence of all the elements as well as

to verify their real contents with the theoretical values in the samples. The theoretical content of Ag w.r.t. Ag-ZnO nanocomposite is 8.7 and 13.7 wt. % for A15 and A25, respectively. However, the real content of Ag in Ag-ZnO nanocomposite as obtained in EDX analysis is 8.6 wt. % and 12.17 wt. % for A15 and A25, respectively. In Fig. 6.7, a clear existence of Ag can be seen in the nanocomposite. Both the samples show sphere-like morphology with an agglomeration in the nanocomposite material. The average grain size of the samples, determined using ImageJ software, are 158 and 114 nm for A15 and A25, respectively.

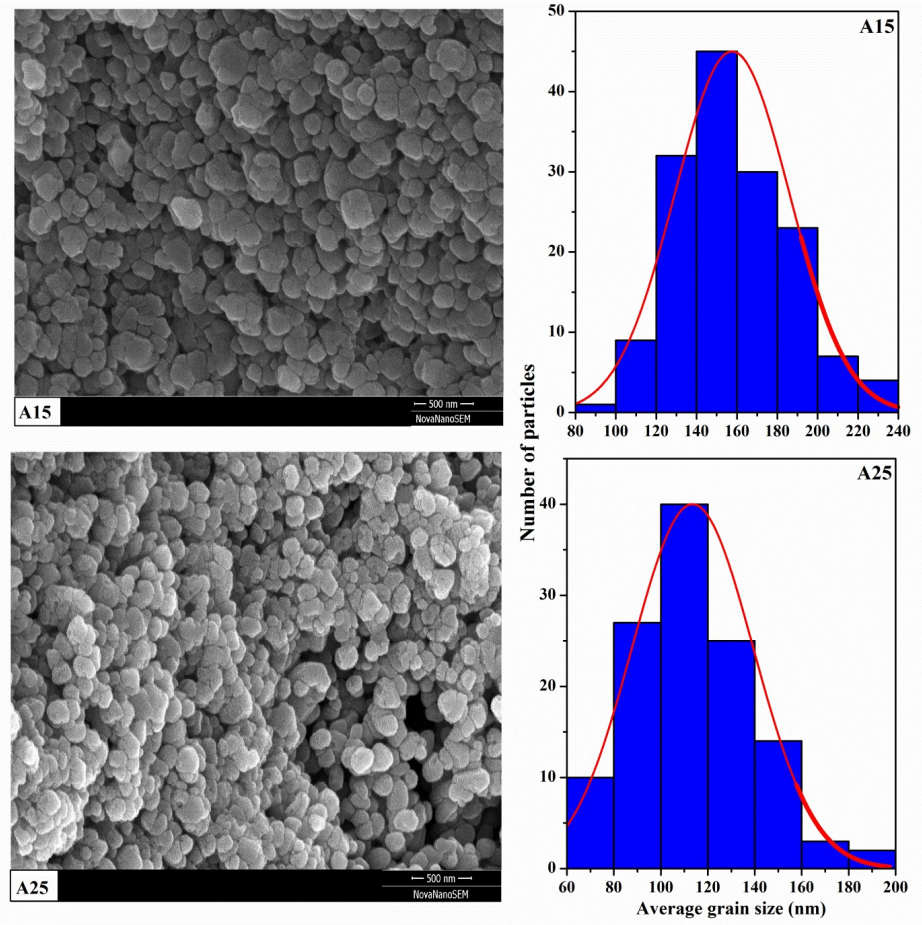


**Fig. 6.6** FE-SEM micrographs and corresponding histograms of A15 and A25.

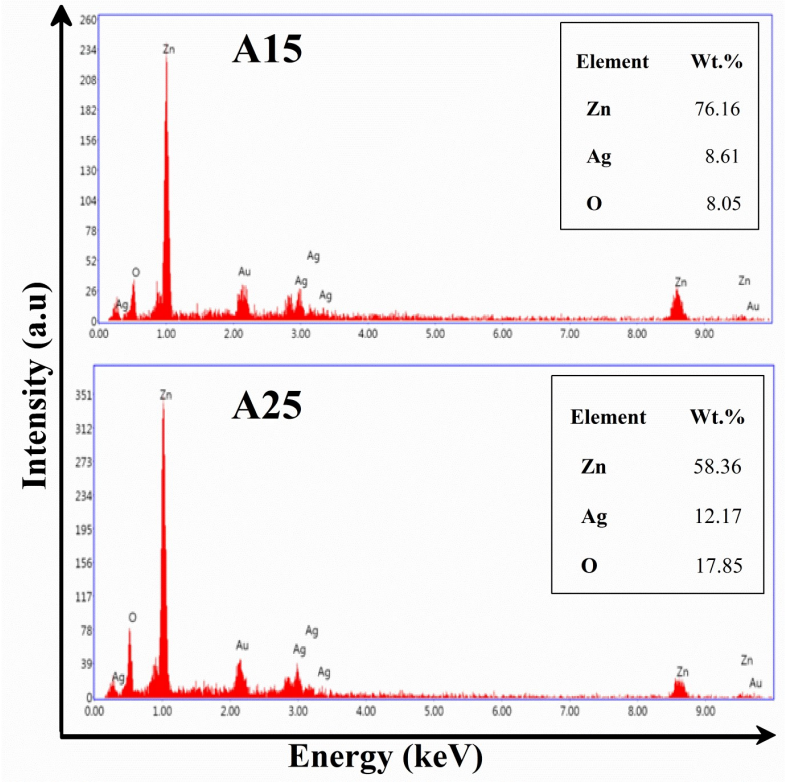


**Fig. 6.7** Energy dispersive X-ray spectrum for A15 and A25.

### 6.4.4 Absorption study

The absorption spectra of the ZnO, A15, and A25 analyzed in the range 200 nm-1000 nm is represented in Fig. 6.8. The peak near 360 nm is assigned to the ZnO band edge absorption [203], whereas the broad absorption peak around 528 nm in the nanocomposite is attributed to the characteristic SPR enhanced absorption, arising due to the near field enhancement and light scattering by sub-wavelength sized metallic Ag-nanoparticles [203,212]. These two characteristic absorption peaks confirm the presence of Ag and ZnO in our samples [201]. The position of LSPR band relies on several factors such as shape, size, and uniformity of metallic nanoparticles as well as the dielectric constant of the surrounding medium [213,214].

To estimate the direct optical band gap ($E_g$) of the samples, the following Tauc relation has been employed [50,215],

$$(\alpha h\nu)^2 = B(h\nu - E_g) \tag{6.16}$$

Where $B$ represents a constant, the absorption coefficient is denoted by $\alpha$ and $h\nu$ stands for the energy of incident photon. The inset in Fig. 6.8 shows the Tauc plot for ZnO. Extrapolation of the linear part of the plot to the energy axis at α=0 provides the optical band gap values, listed in Table 6.5. The estimated bandgap value for ZnO nanoparticles (3.16 eV) is less than that of bulk ZnO, which may be attributed to the strain emerging during the synthesis of nanoparticles [215].

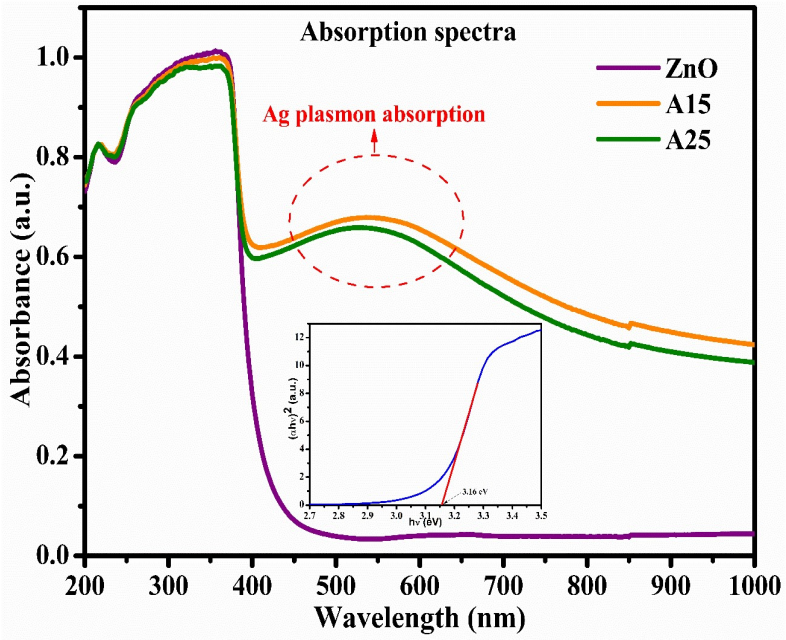


**Fig. 6.8** Absorption spectra for all samples. The nanocomposites show Ag plasmon absorption. The Tauc plot is shown in the inset.

The Urbach energy$E_U$ of the samples have been calculated using the relation [216,217]-

$$\alpha = \alpha_o exp\left\{\frac{h\nu}{E_U}\right\} \tag{6.17}$$

Where $\alpha$ denotes the absorption coefficient, $\alpha_o$ represents a constant, and $h\nu$ denotes the photon energy. The Urbach energy refers to the width of localized state tail in the bandgap region. The $ln(\alpha)$ is plotted against the photon energy $h\nu$ (represented in the inset of Fig. 6.9), and the linear portion of this plot is fitted linearly. The Urbach energy values are then calculated by taking the inverse of the slopes of these linearly fitted straight line portions. The variation of Urbach energy values for all the samples are shown in Fig. 6.9 and the estimated values are summarized in Table 6.5.

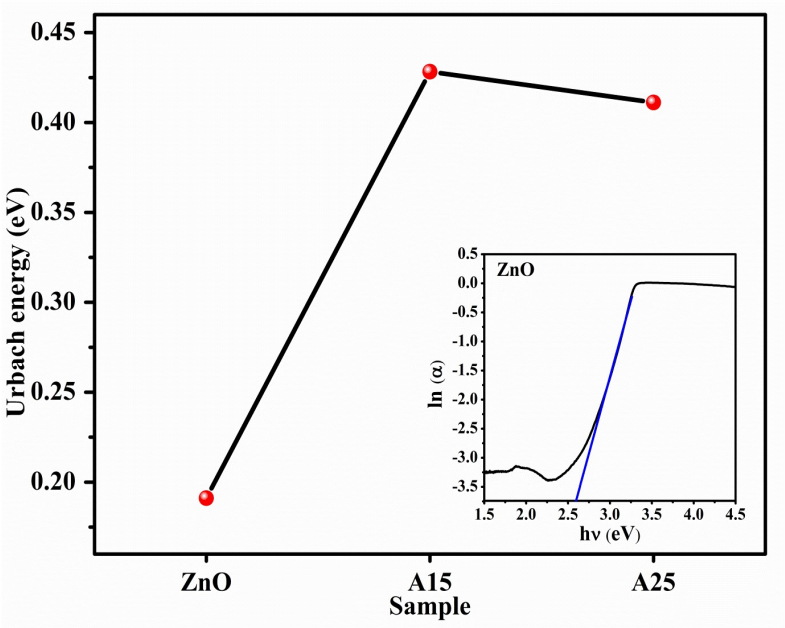


**Fig. 6.9** The comparison of Urbach energy values for all the samples. The inset depicts ln(α) versus hν plot for ZnO.

**Table 6.5** Estimated values of the Band gap, Urbach energy and Responsivity for ZnO and Ag-ZnO nanocomposites.

| Sample | Band gap (eV) | Urbach energy (eV) | Responsivity (A/W) |
|---|---|---|---|
| ZnO | 3.16 | 0.19 | 0.095 |
| A15 | 3.11 | 0.43 | 0.052 |
| A25 | 3.12 | 0.41 | 0.321 |

### 6.4.5 Electrical study

The current-voltage (I-V) characteristics of ZnO, A15 and A25 are shown in Fig. 6.10 (a), have been measured in the applied bias range -2V to 2V under dark and UV illumination (λ= 365nm). Fig. 6.10 (b) depicts the logarithmic plots of the currents for ZnO and nanocomposites, respectively.

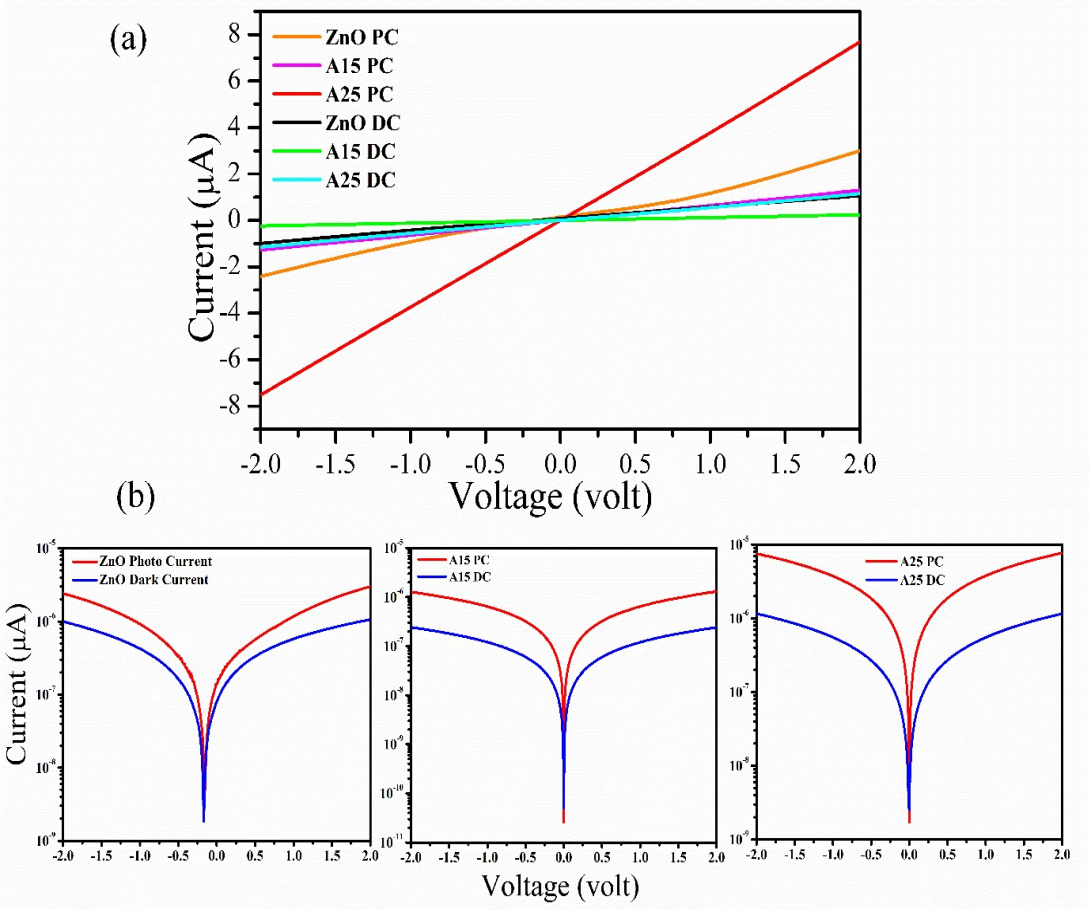


**Fig. 6.10 (a)** Current-voltage (I-V) characteristics of ZnO, A15 and A25 under dark and UV (λ= 365nm) illumination. **(b)** The logarithmic plots of the currents for ZnO and nanocomposites, respectively.(PC = Photocurrent, DC = Dark current)

In the sample A25, a three-fold enhancement in the photocurrent has been observed as compared to the bare ZnO. The photocurrent enhancement of the nanocomposite material as compared to the bare ZnO may be ascribed to the following reasons-

**(a)** The lower value of dislocation density in nanocomposites as collated with the bare ZnO is accredited to the lower crystal defects and higher crystalline nature of the samples, which may arise due to the incorporation of Ag-nanoparticles [196]. Moreover, with the decrease in dislocation density the leakage current decreases and the electron mobility is increased which in turn improves the electrical properties and the performance of Ag-ZnO nanocomposites to make it a suitable candidate for UV photodetectors [181,218].

**(b)** Another reason for the increase in photocurrent could be the increase in the oxygen vacancies in the sample. As the UV photons fall on the sample, electron-hole pairs are generated. The photogenerated holes migrate towards the sample surface, containing negatively charged adsorbed oxygen molecules and get trapped, which results in a decrease in the depletion region. As a result, the quick recombination of electron-hole pairs do not take place easily and the enhanced carrier concentration leads to a higher value of photocurrent. The reduction in microstrain gives the indication of increased oxygen vacancies [219–221].

**(c)** Furthermore, the LSPR of metal nanoparticles increases the absorption of incident UV light inside the ZnO, leading to the generation of a large number of electron-hole pairs and hence the enhanced photocurrent [222].

Responsivity is one of the main characteristics of the photodetectors and can be calculated using the formula [223,224],

$$R = \frac{I_{light} - I_{dark}}{P * S} \tag{6.18}$$

Where, $I_{dark}$ and $I_{light}$ denote the dark and photo-currents, respectively. P stands for the optical power density and an effective area of the device is denoted by S.

The estimated values of the responsivity for ZnO and nanocomposites at 2V are tabulated in Table 6.5. An evident enhancement in the responsivity values in A25 clearly indicates that this composition is more suitable for the photodetector application.

### 6.5 Conclusions

In this chapter, ZnO and Ag-ZnO nanocomposites have been synthesized by facile precipitation method. The work is mainly focussed on the detailed structural analyses of ZnO and its various nanocomposites comprised of silver metal nanoparticles. The structural analysis ascertains the formation of ZnO nanoparticles and Ag-ZnO nanocomposites with good crystallinity and without any impurity and also decrease in strain and stress for A25 nanocomposites is observed by increasing higher concentration of Ag nanoparticles. UV-Vis spectrum clearly shows a broad peak attributed to the SPR enhanced absorption due to Ag- nanoparticle. FE-SEM and EDX analysis have been carried out for the morphological and elemental analysis. Moreover, the current-voltage (I-V) characteristics of all samples have been measured under dark and incident UV illumination. Upon UV illumination, a clear enhancement in the photocurrent in the sample A25 is observed which is ascribed to the reduced microstrain and the LSPR phenomena. Our study corroborates that A25 is a suitable candidate for UV-photodetectors.